Contents lists available at ScienceDirect

Journal of Magnetic Resonance

journal homepage: www.elsevier.com/locate/jmr





Frame change technique for phase transient cancellation

Andrew Stasiuk a,b,*, Pai Peng c, Garrett Heller d, Paola Cappellaro a,b,d

- a Department of Nuclear Science and Engineering, Massachusetts Institute of Technology, Cambridge, 02139, MA, USA
- ^b Research Laboratory of Electronics, Massachusetts Institute of Technology, Cambridge, 02139, MA, USA
- ^c Department of Electrical and Computer Engineering, Princeton University, Princeton, 08544, NJ, USA
- d Department of Physics, Massachusetts Institute of Technology, Cambridge, 02139, MA, USA

ARTICLE INFO

Keywords: Nuclear magnetic resonance Solid-state NMR Fluorapatite High-fidelity control Pulse error cancellation

ABSTRACT

The precise control of complex quantum mechanical systems can unlock applications ranging from quantum simulation to quantum computation. Controlling strongly interacting many-body systems often relies on Floquet Hamiltonian engineering that is achieved by fast switching between Hamiltonian primitives via external control. For example, in our solid-state NMR system, we perform quantum simulation by modulating the natural Hamiltonian with control pulses. As the Floquet heating errors scale with the interpulse delay, δt , it is favorable to keep δt as short as possible, forcing our control pulses to be short duration and high power. Additionally, high-power pulses help to minimize undesirable evolution from occurring during the duration of the pulse. However, such pulses introduce an appreciable phase-transient control error, a form of unitary error. In this work, we detail our ability to diagnose the error, calibrate its magnitude, and correct it for $\pi/2$ -pulses of arbitrary phase. We demonstrate the improvements gained by correcting for the phase transient error, using a method which we call the "frame-change technique", in a variety of experimental settings of interest. Given that the correction mechanism adds no real control overhead, we recommend that any resonance probe be checked for these phase transient control errors, and correct them using the frame-change technique.

1. Introduction

As a fairly mature technology, nuclear magnetic resonance (NMR) provides easy access to systems which evolve under quantum mechanical equations of motion. In particular for solid-state systems, multiple-pulse experiments were introduced to increase the spectral resolution, thereby extracting more information about a sample [1,2]. Additionally, solid-state NMR provides access to strongly interacting quantum systems with T_1 times on the order of seconds, which is of interest for condensed matter theory. The accessible dynamics of these systems are greatly expanded via the Hamiltonian engineering toolbox, wherein periodic application of pulse sequence gives rise to average evolution under a desirable target Hamiltonian [3-6]. Proper utilization of these techniques situates solid-state NMR as a leading method for analog quantum simulation. Of vital importance is ensuring that the simulated dynamics does not differ too much from the target dynamics. Achieving high-fidelity simulations and measuring highresolution spectra requires good hardware, a well calibrated device, and well designed pulse sequences [7,8].

As early as the 1970s, it was realized that attempts to produce square pulses for the purpose of radio-frequency quantum control led to electronic "phase glitches", more commonly known as phase transients, as a result of non-linear circuit elements [9]. Namely during the rise and fall time of an RLC circuit under a non-ideal square pulse voltage driving, there is a naturally occurring out-of-phase contribution to the magnetic field experienced by the spins in the rotating frame [2,10]. Investigations of this effect were later extended from simple RLC circuits to parallel-tuned, series-matched probe circuits to better model NMR systems [11]. It has been repeatedly found, and indeed it is expected, that the actual phase transient is larger in magnitude than the electronic analysis would otherwise predict [10,11].

Early solutions to correcting for the effects of phase transients were predicated on the symmetry of the magnitude of the leading and trailing edge errors [2]. In these older systems, the relative magnitude of these leading and trailing terms could be more readily controlled via modification of the quiescent base currents of transistors within the probe electronics [2]. Other factors affecting the fine details of phase transient include the O factor of the probe, relative detunings, and impedance mismatches [9-11]. To improve the performance of NMR spectrometers in light of these errors, multi-pulse sequences with particular symmetries were shown to be partially robust to phase-transients of a particular sign symmetry [2]. Other pulse sequences were modified to better correct for phase transient errors, often extending the Floquet

Corresponding author at: Department of Nuclear Science and Engineering, Massachusetts Institute of Technology, Cambridge, 02139, MA, USA. E-mail address: astasiuk@mit.edu (A. Stasiuk).

period of a given cycle. The XY-4,8,16 pulse sequence family are an illustrative example of this methodology applied to CPMG [12–14].

Modern spectrometers have less control over the relative magnitude of the leading and trailing phase transients, with the general assumption being that they are equal in magnitude, but may possibly differ in sign [15–18]. Vega demonstrated that with careful tuning of the resonance probe, one can significantly mitigate the effect of phase transients while allowing for a very general error model [16]. This technique appears to work very well if one is able to measure a sufficiently narrow spectrum which is sensitive to the detuning, and has the ability to freely change the detuning without loss of performance. Weber et al. demonstrated that, under an abstract pulse error model reminiscent of Mehring and Waugh's pioneering analysis, one can attempt to optimize the phase of a single pulse in a sequence to reduce the effect of phase transients [18]. These phase transient-adapted pulse sequences also appear to work quite well, but the calibration step requires optimizing the performance of a particular sub-cycle as function of a phase offset.

Via pulse shaping, the phase transient can be nearly entirely limited. The core notion underpinning this technique is an idea known as "active compensation" [19]. Here, the goal is to calibrate the response function of the resonance probe in order to then design a pulse shape which leads to the desired response, e.g. a square wave [17]. In order to calibrate the probe's response function, however, one must directly measure its transient response to driving via a nearby pick-up coil. These optimal control theory techniques have been very successful. especially in high-Q resonators [15,20,21]. All else being equal, a pulseshaped solution will have a longer duration than an unmodified square pulse. When the goal is to shape the system dynamics via Hamiltonian engineering, such longer pulse lengths are usually detrimental and increase the error in generating a desired time-average target Hamiltonian. To minimize the Trotter error during an evolution of length $T = n\delta t$, one takes each Trotter step δt to be as short as possible. This in turn implies that the delays within a Floquet cycle designed to produce a target Hamiltonian should also be as short as possible. The physical limitations that prevent $\delta t \longrightarrow 0$ are finite pulse lengths and electronic switching times. By taking δt to be as short as our control allows, we introduce significant phase transient errors into individual pulses. We still find that longer, albeit higher fidelity, square pulses perform worse than short, high-power pulses for complex Hamiltonian engineering tasks.

Here we show how to overcome this challenge by canceling the phase transient error for $\pi/2$ -pulses. Importantly, we take a "black-box" approach to the fine details of the magnetic fields applied to the nuclear spins. That is, we motivate an effective unitary error model based on what is expected from existing literature, and simplify it for the case of our specific setup. This allows us to tune up our error model parameter to high precision and ensure a our calibration procedure is fast and efficient.

Our correction protocol utilizes virtual-z gates, which allow for high fidelity rotations with 0 pulse length [22,23]. These virtual-z gates have been utilized in NMR to introduce static fields [24] and in superconducting quantum platforms to cancel off-resonant control errors [22]. Inspired by their usage in superconducting devices, we calibrate our unitary pulse error stemming from the phase transient with a simple experiment, and correct it using only virtual-z rotations. This method is exact under the assumption that the phase transient is dominated by a single edge contribution (either leading or trailing), which we believe is the case in our system. For balanced phase transient errors, our proposed solution corrects the phase transient error to second order. We detail this extension of our technique to the more general case at the end of the next section. In this work we detail how to calibrate and correct the phase transient error in-situ, and demonstrate its utility in an array of Hamiltonian engineering experiments via fidelity-like measurements.

2. Methods

We focus on controlling an ensemble of solid-state fluorine-19 nuclear spins with resonant radio-frequency (rf) driving. Our sample is single crystal of fluorapatite, $\text{Ca}_5(\text{PO}_4)_3\text{F}$, placed in a single resonance probe which is tuned to the fluorine Zeeman frequency of \sim 282 MHz. The probe is controlled by an aging, piecemeal, 300 MHz (\sim 7T) Bruker Avance spectrometer using a BLAX300RS amplifier and an HPPR preamplifier. The fluorapatite sample is oriented so that the magnetic field is aligned along the crystal c-axis in order to maximize nearest-neighbor fluorine-fluorine coupling strength. As usual, our control induces the following Hamiltonian in the rotating frame,

$$\mathcal{H}_{c}(t) = f(t) \left(\cos(\phi) \hat{S}_{x} + \sin(\phi) \hat{S}_{y} \right), \tag{1}$$

for collective spin operators \hat{S}_{μ} , $\mu \in \{x,y,z\}$. The function f(t) is ideally a train of square pulses of fixed length and power, each resulting in a net $\pi/2$ rotation about the transverse axis determined by ϕ , which has a resolution of one degree.

In reality, true square pulses are impossible to generate, as there is a finite rise and fall time when turning on and off a voltage source. The already imperfect shape will enter into the resonance probe, which has a finite Q, adding an additional rise and fall time structure to the pulse shape. It was found that during the leading and trailing edges, an out-of-phase current component is induced in the resonance probe circuit [9,11]. The magnitude and relative ratio of these leading and trailing phase transients is balanced if the pulse shape entering the probe circuit has a rise and fall times which are much smaller than the natural rise and fall times of the RLC system. We assume that this is the case in our system based on experimental evidence shown later in this paper. In general, we adopt the following broad error model for a non-ideal $\pi/2$ x-pulse:

$$\hat{U}_{err} = e^{i\phi_e \hat{S}_z} e^{-i\theta_{tr} \hat{S}_y} e^{-i(\pi/2 + \epsilon)\hat{S}_x} e^{-i\theta_l \hat{S}_y} e^{-i\phi_e \hat{S}_z}. \tag{2}$$

For a spin with gyromagnetic ratio γ , these constants error constants can be computed assuming perfect knowledge of the control fields $B_x(t)$ and $B_y(t) = B_y^l(t) + B_y^{r}(t)$. For the out of phase *y*-field, we split the time dependence into a leading (*l*) and trailing (*tr*) component. Concretely,

$$\epsilon = \frac{\pi}{2} - \int_0^{t_p} dt B_x(t) \tag{3}$$

$$\theta_{l/tr} = \int_0^{t_p} dt B_y^{l/tr}(t). \tag{4}$$

Thus, ϵ is the over-rotation angle, $\theta_{l/lr}$ are the leading/trailing phase transient rotations, and ϕ_e is a phase error that corresponds to an inplane twisting of the rotation axis from x by an angle ϕ_e . This complete error model is similar to the 4-pulse error model taken by Vega [16]. For this work, we will assume ϵ and ϕ_e are zero. Indeed, we can consider such errors to be due to an imperfect tune-up procedure, rather than an intrinsic physical limitation of our control capabilities. What remains are the leading and trailing phase transients, a 2-pulse error model.

We find that for short $\pi/2$ pulses, $t_p < 2.5~\mu s$, there is a noticeable phase transient contribution. Somewhat surprisingly, we find that the phase transient contribution is dominantly seen in the leading edge (see Fig. 1 and Appendix A). That is, we believe we have a single-pulse error model in our system. For an arbitrary rotation axis denoted by ϕ , our experimental unitary is as follows:

$$U_{\phi} = R_{\phi}(\pi/2) \longrightarrow U_{exp} = R_{\phi}(\pi/2)R_{\phi+\pi/2}(\theta_{fc}), \tag{5}$$

where

$$R_{\phi}(\theta) = \exp\left(-i\theta\left(\cos\phi\hat{S}_x + \sin\phi\hat{S}_y\right)\right). \tag{6}$$

A solely leading edge phase transient has been observed before [9] or achieved by tuning [11].

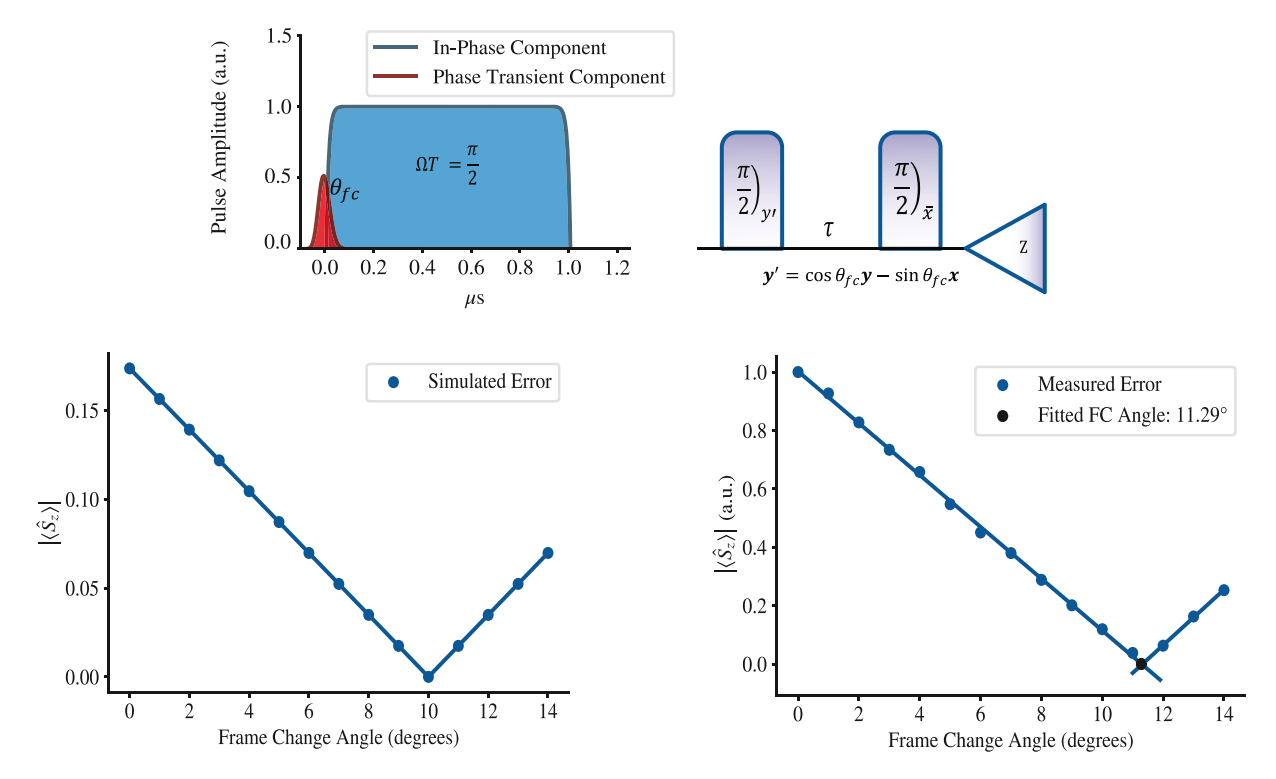


Fig. 1. Schematic of the phase transient introduced by short square pulses (top-left), and the experimental sequence to determine $\theta_{f\varepsilon}$ (top-right). If there were no phase transient error, then we would expect to measure $\langle \hat{S}_z \rangle = 0$. By varying the deflection angle from the y-axis of the first pulse, we can experimentally determine $\theta_{f\varepsilon}$ by finding the angle which minimizes $\langle \hat{S}_z \rangle$. In the bottom-left, we show the theoretical prediction for this error model when $\theta_{f\varepsilon} = 10^{\circ}$, along with experimental data (bottom-right) which demonstrates a measured $\theta_{f\varepsilon} \approx 11^{\circ}$.

To experimentally determine θ_{fc} , we perform a simple experiment in which we apply a $\pi/2$ pulse about an axis which is rotated θ from y, then rotate by $\pi/2$ about \bar{x} to transfer the error into z, and finally measure the z magnetization. We repeat this process, iterating θ , and find the point of no error by transforming the root finding problem to a minimization problem. The procedure is further detailed in Fig. 1, where we also demonstrate that our observed data closely matches the simulated model. We have found that the calibrated θ_{fc} changes slightly after re-tuning the probe and spectrometer. Namely, for a given tuning and matching of the resonance probe and frequency offset, we calibrate the $\pi/2$ power for a given pulse length, which then fixes the frame-change angle. This angle is stable until we re-tune, usually in accordance with large external temperature and humidity fluctuations, or drifts of the static field.

Once θ_{fc} is calibrated, the error can be corrected by noting the following identity:

$$R_z(\mp\theta_{fc})R_\phi(\pi/2)R_{\phi\pm\pi/2}(\theta_{fc}) = R_\phi(\pi/2).$$
 (7)

Thus, the out-of-phase over-rotation error can be completely canceled via a repeated z rotation after each electronically generated pulse.

Since a *z*-rotation of angle θ is performed by phase shifting all subsequent pulses by θ , our method for error correction is achieved by an increasing phase shift, whereby the *n*th pulse is shifted by an angle $(n-1)\theta_{fc}$ from its original value. This is pictorially shown in Fig. 2. Our method can be thought of as a discrete version of a rotating frame transformation, and we call θ_{fc} the "frame-change" angle. In the next section, we will demonstrate the improvements gained from correcting for this error.

Finally, we note that this technique still works, albeit approximately, if the phase transient error is balanced over the leading and trailing edge. It has previously been shown that arbitrary phase transient error results in a slight deviation of the rotation axis into the z-direction [9]. Concretely, for a desired $\pi/2$ x-rotation, the experimental

unitary is modified as

$$R_x(\pi/2) \longrightarrow U_{alt} = \exp\left(-i\frac{\pi}{2}\left(\hat{S}_x + \epsilon_{fc}\hat{S}_z\right)\right).$$
 (8)

Using the second-order Suzuki-Trotter decomposition [25], we can show that adding a leading and trailing virtual-z rotation corrects for ϵ_{fc} ,

$$\log\left(R_z(\theta_{fc}/2)\exp\left(-\mathrm{i}\frac{\pi}{2}\left(\hat{S}_x + \epsilon\hat{S}_z\right)\right)R_z(\theta_{fc}/2)\right) = -\mathrm{i}\frac{\pi}{2}\hat{S}_x + O(\epsilon^2), \quad (9)$$

with $\theta_{fc}=-\frac{\pi}{2}\epsilon$. Hence, even in the worst case where the leading and trailing phase transients are equal in magnitude, our correction technique still works, with the caveat that the correction quality scales with the square of the relative phase transient error.

3. Results and discussion

We evaluate the performance of the frame-change technique by measuring improved fidelity in Hamiltonian engineering and longer-lived signals in dynamical decoupling experiments. Indeed, across a wide range of experimental settings, by correcting the out-of-phase over-rotation error the frame-change technique leads to improved signal lifetimes. We demonstrate this effect in time-suspension experiments, Loschmidt echo (time reversal) experiments, and spectral sequence experiments.

In addition, we perform these experiments for multiple pulse lengths. Generally, the shorter the pulse length, the higher the required power, which in turn results in a larger θ_{fc} . This trend is consistent with the existing literature's conclusions on the electronic origins of the phase transient [2]. However, shorter pulses also allow for shorter delays during Floquet engineering, leading to smaller errors in simulating a target Hamiltonian [7,8]. We will clearly demonstrate that cancellation of the phase transient error via the frame-change technique allows for higher resolution experiments at equivalent pulse lengths.

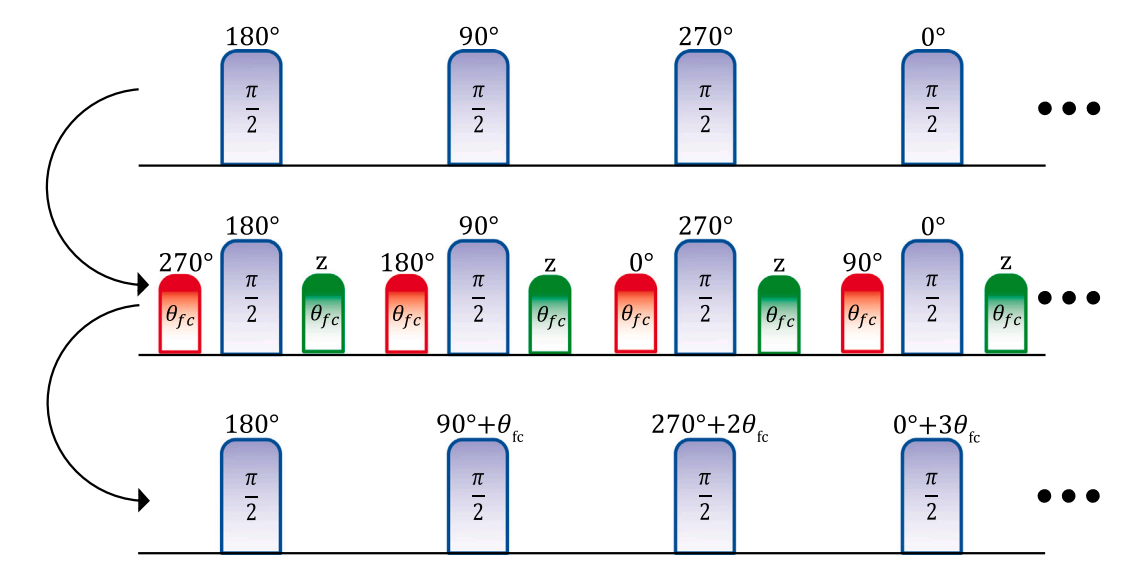


Fig. 2. Schematic representation of the frame-change technique, applied to a WAHUHA-like pulse sequence. On the top, we show the *logical pulse sequence*, a series of $\pi/2$ pulses of arbitrary phases. We then include the phase transient error (red), and the necessary frame-change correction z-rotations (green), to form the *detailed pulse sequence* (middle). Finally, we compile the z-rotations, which implicitly cancel the errors, resulting in the *experimental pulse sequence* (bottom), which implements the logical pulse sequence and cancels the phase transient errors.

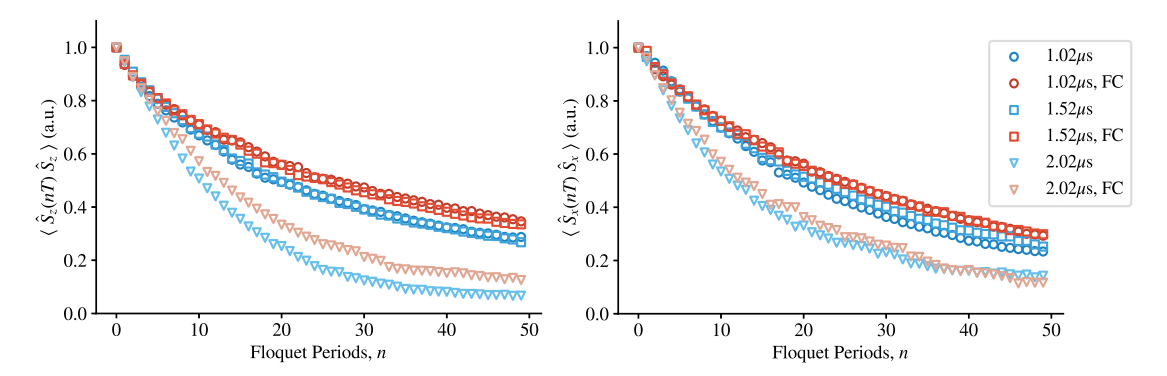


Fig. 3. Comparison of the fidelity of Peng24 time suspension sequences with (red) and without (blue) frame-change correction in both the longitudinal (left) and transverse (right) directions. For pulse lengths of 1.02 μs and 1.52 μs, we use the delay primitive $\tau = 5$ μs, leading to a Floquet period of 120 μs. For $t_p = 2.02$ μs, the delay primitive must be increased to $\tau = 6$ μs, leading to a larger error term manifesting in a signal of significantly reduced magnitude.

However, it will also be clear that minimizing the Trotter error has a greater impact on achieving high-fidelity evolution under a target time-averaged Hamiltonian. Hence, short, high-power pulses using the frame-change technique offer the highest performance possible on our hardware.

In Fig. 3, we demonstrate that under the Peng24 time suspension sequence [5], the frame-change correction leads to a slower decay, for various pulse lengths $t_p=1.02,1.52,2.02~\mu s$. Peng24 was specifically designed to be robust to unitary errors, so one might think that the frame-change technique would not show a significant improvement [5]. However, the phase transient-induced error is markedly different than a simple over-rotation error, and we find that correcting for this error can still provide meaningful improvements in the signal lifetime. Even if a pulse sequence was designed to cancel the phase-transient error over its Floquet period, such cancellation would likely still be imperfect, and thus benefit from the addition of the frame-change technique.

Generally, including the frame-change technique should not reduce the signal fidelity. However, the magnitude of improvement can be variable depending on the sequence and the quadrature of measurement. Indeed, this effect is even more pronounced if we consider Angle12, a time suspension sequence consisting of only the first half of Peng24 [5]. This sequence has no reflection symmetry, and thus *a priori* one would expect it to have worse error scaling than Peng24. The results of this experiment are shown in Fig. 4.

Next, we analyze a case in which including frame-change corrections results in a decrease in signal magnitude, but an increase in the simulation fidelity. For this, we utilize the MREV-8 spectral sequence, which cancels the dipolar interaction, but leaves a residual disordered field term [4,26]. We choose MREV-8 over other spectral sequences, such as symmetrized WAHUHA, because the resulting disordered field points along the $\frac{1}{\sqrt{2}}(x+z)$ axis (with scaling factor $\sqrt{2}/3$). Thus, we a priori expect measurements in the x and z quadrature to be equal. Indeed, under the assumption of quenched disorder, with h_i distributed as a Gaussian with 0 mean and variance σ_h^2 , we compute

$$\overline{\left\langle \hat{S}_{z}(t)\hat{S}_{z}\right\rangle} = \overline{\left\langle \hat{S}_{x}(t)\hat{S}_{x}\right\rangle} = \frac{1}{2} + \frac{1}{2}e^{-\frac{1}{9}(\sigma_{h}t)^{2}}.$$
 (10)

Details of this calculation are given in Appendix B. In Fig. 4, we show the results of these measurements, with and without frame change corrections, along with the analytic prediction.

To understand the over-prediction of the z-measurements, we recall that the net effect of a general phase transient error, integrated over the duration of the pulse, is a deflection of the rotation axis towards the z-direction, with the sign of the deflection depending on the details of the phase transient [10]. Hence, to leading order, this error induces a Trotterized field along z over each Floquet period. In total, the effective field felt by each spin is

$$\boldsymbol{B}_{\epsilon}^{(i)} = \frac{1}{3}h_{i}\boldsymbol{x} + \frac{1}{3}(h_{i} + 3h_{\epsilon})\boldsymbol{z},\tag{11}$$

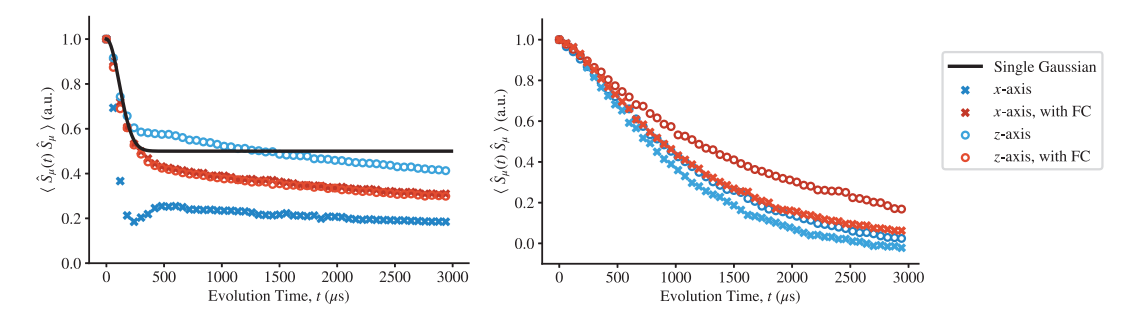


Fig. 4. On the left, we show a comparison of analog quantum simulation results with (red) and without (blue) the frame-change correction for pulse length $t_p = 1.02$ µs under MREV-8. Additionally, we include the analytic prediction (black), showing good coincidence with the frame-changed corrected experimental data. On the right, we show the evolution under the Angle12 time suspension sequence, which has poorer Trotter error scaling than Peng24, leading to a more pronounced difference than shown in Fig. 3.

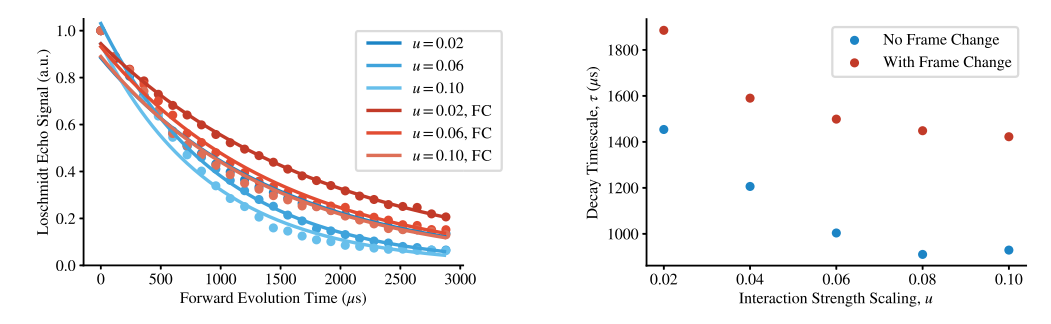


Fig. 5. Effect of the frame change technique on a Loschmidt echo experiment. On the left, we show the signal as a function of the forward evolution time for select interaction scalings, u. Experiments (not) using the frame change technique are plotted in red (blue), along with their fits to the model $S(t) = A \exp(-(t/\tau))$. On the right, we plot the decay timescale τ as a function of the interaction scaling parameter u. Notice that the inclusion of the frame change technique leads to the Loschmidt echo to decaying more slowly than the results from evolving under the uncorrected sequence.

where h_{ε} is the magnitude of the field generated by the phase transient error over a single Floquet period. This implies that magnetization along z is "more conserved" than it otherwise should be, thanks to an emerging symmetry. Conversely, the x magnetization is not protected (its fast decay prevents us from observing oscillations due to h_{ε}). These measurements conclusively show that the frame change technique is capable of significantly improving the simulation fidelity, as evidenced by the coincidence of $\langle \hat{S}_z(t)\hat{S}_z \rangle$ and $\langle \hat{S}_x(t)\hat{S}_x \rangle$ with frame change corrections.

In addition to time suspension and dipolar decoupling sequences, we analyze Hamiltonian engineering pulse sequences which result in a non-zero target Hamiltonian. To evaluate the control performance in this case, we measure the Loschmidt echo. The Loschmidt echo is a fidelity-like measurement linked to irreversibility and quantum chaos, which encodes our ability to reverse Hamiltonian evolution [27]. For this investigation, we use Wei16 to engineer the double quantum Hamiltonian for a variety of interaction strengths, and measure the Loschmidt echo under time reversal [24]. Concretely, the double quantum Hamiltonian is given in Eq. (12) below.

$$\mathcal{H}_{DQ} = \frac{u}{2} \sum_{i \le j} J_{ij}^{FF} \left(\hat{S}_x^{(i)} \hat{S}_x^{(j)} - \hat{S}_y^{(i)} \hat{S}_y^{(j)} \right)$$
 (12)

Using Wei16, the interacting scaling parameter u can be varied and made negative. For these experiments, the sign of the interaction term is made negative by transforming the phases of the pulses in the Hamiltonian engineering sequence, namely via a reflection which maps $x\leftrightarrow y$ and $\overline{x}\leftrightarrow \overline{y}$. This ensures all interpulse delays are unchanged relative to the forward and backward evolution steps, leading to a more uniform error term across the entire experiment and a higher overall fidelity. Additional details of the Wei16 sequence can be found in Appendix C. The experimental data is shown in Fig. 5, and demonstrates a significant improvement in the Loschmidt echo decay timescale for frame-change corrected sequences of all interaction magnitudes.

4. Conclusion

In this work, we have demonstrated our ability to diagnose and correct for unitary error caused by short, high power, unitary control. Given the electronic origin of the phase transient error, we expect that this error modality extends to all resonant probe-type devices. We argued that avoiding previously utilized solutions such as pulse-shape engineering is advantageous for quantum simulations tasks in order to keep control pulses as short as possible. Indeed, we found better Hamiltonian engineering and time suspension performance at shorter pulse lengths, as we were able to more effectively reduce Trotter error. Since shorter pulses require higher power, this "Trotter-optimal" control results in larger phase transient errors, which we are then able to correct using the frame-change technique to ensure we perform high fidelity pulse sequences.

We applied the frame-change technique to multiple Hamiltonian engineering experiments, including time suspension and time reversal. We found that the error-corrected sequences never reduce the signal fidelity, and almost always outperformed the uncorrected sequences. Indeed, we have previously utilized the frame change technique to enable novel quantum simulation experiments on nuclear spins, such as the observation of a prethermal U(1) time crystal [28].

In this work, we used a simplified error model in which the phase transient is entirely located on the leading edge of our pulse. This simplification is well motivated on our spectrometer. More broadly, when the phase transients are balanced on the leading and trailing edge, the frame-change technique still perturbatively corrects for this error. Additionally, we note that while we focused on Hamiltonian engineering sequences which only utilize $\pi/2$ -pulses, our central identity in Eq. (7) applies to arbitrary rotation angles, not just $\pi/2$ -rotations. An interesting direction for future research would be to understand the phase transient magnitude as a function of rotation angle, so that our procedure could be extended to a broader class of Hamiltonian engineering sequences.

CRediT authorship contribution statement

Andrew Stasiuk: Writing – original draft, Visualization, Validation, Methodology, Investigation, Formal analysis, Data curation. Pai Peng: Writing – review & editing, Methodology, Conceptualization. Garrett Heller: Investigation, Data curation. Paola Cappellaro: Writing – review & editing, Supervision, Resources, Project administration, Funding acquisition, Conceptualization.

Declaration of competing interest

The authors declare the following financial interests/personal relationships which may be considered as potential competing interests: Andrew Stasiuk reports financial support was provided by National Science Foundation. Andrew Stasiuk reports financial support was provided by Laboratory for Physical Sciences. If there are other authors, they declare that they have no known competing financial interests or personal relationships that could have appeared to influence the work reported in this paper.

Data availability

Data will be made available on request.

Acknowledgments

We thank Alex Ungar and Santiago Hernández-Gómez for helpful discussions which enabled this work. This work was supported in part by the National Science Foundation, United States under Grants No. PHY1915218 and No. PHY1734011, and the CQE-LPS Doc Bedard Fellowship.

Appendix A. Electronic origins of pulse error

It has been previously shown with careful circuit analysis that the phase transient is due to finite rise and fall times of the electronic signal generated by the NMR spectrometer [10,11] and their interplay with the resonant probe circuit. For a simple circuit model, Ellet et al. showed that given an incident electronic signal e(t) and circuit impedance Z(s), the current in the inductor producing the rf control pulses is given by an inverse Laplace transform of the ratio of these quantities [10]. Namely,

$$i(t) = \mathcal{L}^{-1} \left[\mathcal{L}[e(t)](s) / Z(s) \right], \tag{A.1}$$

where \mathcal{L} denotes the Laplace transform, and \mathcal{L}^{-1} its inverse. Via this analysis, the phase transient is a simple consequence of a non-constant electronic signal amplitude. Assuming a perfectly square pulse is sent into the probe, the Q of the probe circuit will lead to a finite rise and fall time, which must be symmetric. In this case, the phase transient on the leading and trailing edge are equal in magnitude. If an imperfect square pulse is sent into the probe with a rise/fall time which is longer than the probe's rise/fall time, then this timescale will dominate the dynamics, and would lead to unequal leading and trailing phase transients.

Without the invasive approach of using a pick-up coil to directly measure the phase transient generated in the probe circuit, as has been done previously [17,19], we can still attempt to understand the incident pulse shape generated by the spectrometer. To do this, we use a Lecroy Waverunner 104Xi-A 1 GHz oscilloscope to measure the voltage signal produced by the NMR spectrometer. Due to technical considerations, we passed the signal through a large attenuator and long transmission line before measurement, which introduced additional sources of electronic noise. To generate a clean signal, we performed a simple moving average on the signal with a delay kernel of 100 data points, corresponding to a real-time window of 0.01 μs . Since this window is small compared to the overall pulse length, we do not expect that this

averaging will meaningfully impact the pulse shape details. The results of these measurements are shown in Fig. A.6.

It is apparent from Fig. A.6 that the rise-time is an increasing function of pulse power. Hence, the proportion of time spent with a time varying signal amplitude for a short high-power pulse is much larger than in a longer and lower-power pulse. This coincides with the observed trend that the shortest considered pulse has the largest phase transient error, and monotonically decreases with increasing pulse length. Hence, we argue that since the observed rise-time of the spectrometer-generated pulse-shape is significantly longer than the falltime, the phase transient error can be well approximated as occurring only on the leading edge. This is captured by the unitary error model given in the main text in Eq. (5). The source of this imbalanced effect must then stem from non-linear circuit elements during amplification and signal generation. Given the volume of literature which assumes and/or measures balanced phase transient errors [16-18], such an imbalance seems fairly uncommon. Our spectrometer is quite old, and many of the components have been replaced over the past few decades, which may contribute to the observed long rise-time.

Appendix B. Evolution under MREV-8

The MREV-8 sequence on a solid state sample cancels the homonuclear dipolar interaction, while allowing for a residual local field [4, 26]. Namely, the heteronuclear dipolar interaction of the phosphorus and fluorine spin in fluorapatite can be rewritten as local field generated by nearby phosphorus spins in fluorapatite. Concretely, this interaction is of the form

$$\mathcal{H}_{dis} = \sum_{i,j} J_{ij}^{FP} \hat{S}_{z}^{(i)} \hat{I}_{z}^{(j)} \approx \sum_{i} h_{i} \hat{S}_{z}^{(i)}, \tag{B.1}$$

where the interaction strength is

$$J_{ij}^{FP} = \frac{\hbar^2 \gamma_F \gamma_P (1 - 3\cos^2(\theta_{ij}))}{\|r_i - r_j\|^3},$$
(B.2)

with $\gamma_{F,P}$ the gyromagnetic ratios of the F and P spins, $r_{ij} = r_i - r_j$ the vector joining the two spin locations and θ_{ij} the direction of r_{ij} with respect to the external magnetic field.

The heteronuclear dipolar interaction is then transformed to an effective disordered field model

$$\mathcal{H}_{MREV} = \frac{1}{3} \sum_{i} h_i (\hat{S}_x^{(i)} + \hat{S}_z^{(i)}). \tag{B.3}$$

We treat the system as having quenched disorder, since the timescale of the evolution of the phosphorus spins exceeds the experimental timescales of interest. In other words, h_i is treated as a random value with statistics determined by the spin temperature and crystal geometry, rather than a collection of spin operators.

By treating the disorder as fixed during a single experiment, we can independently compute the evolution of each spin and average over the distribution of the disordered field. Then,

$$\hat{S}_{z}^{(i)}(t) = \exp(-it\mathcal{H}_{MREV})\hat{S}_{z}^{(i)}\exp(it\mathcal{H}_{MREV}), \tag{B.4}$$

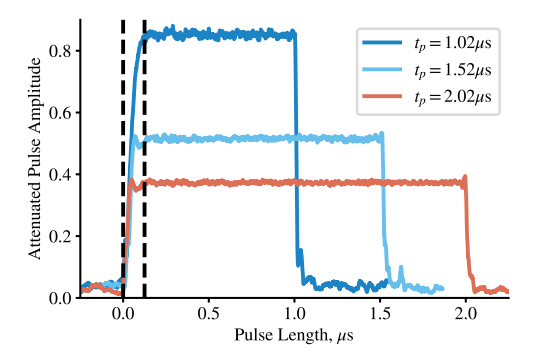
which can be exactly computed,

$$\hat{S}_{z}^{(i)}(t) = \frac{1}{2} \left(1 + \cos \frac{\sqrt{2}h_{i}t}{3} \right) \hat{S}_{z}^{(i)} + \frac{1}{2} \left(1 - \cos \frac{\sqrt{2}h_{i}t}{3} \right) \hat{S}_{x}^{(i)} - \frac{\sqrt{2}}{4} \sin \frac{\sqrt{2}h_{i}t}{3} \hat{S}_{y}^{(i)}.$$
(B.5)

Relevant to our experiments, we can easily compute two-point infinite temperature correlator,

$$4\left\langle \hat{S}_{z}^{(i)}(t)\hat{S}_{z}^{(i)}\right\rangle = \frac{1}{2}\left(1+\cos\frac{\sqrt{2}h_{i}t}{3}\right). \tag{B.6}$$

By symmetry, we would get the same result for $\langle \hat{S}_x(t)\hat{S}_x \rangle$ after a repeat of the above computation.



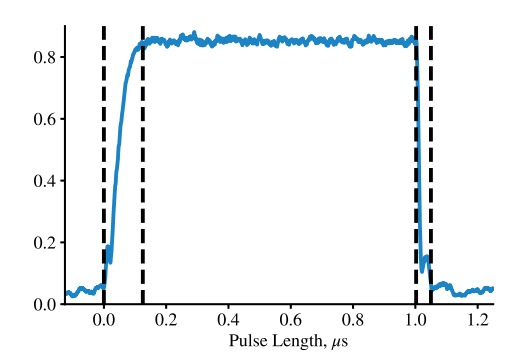


Fig. A.6. Oscilloscope measurements of $\pi/2$ -pulses generated by the NMR spectrometer, smoothed with a simple moving average to reduce electronic noise, for $t_p \in \{1.02, 1.52, 2.02\}$ μs. On the left, we denote the start and end of the rise-time for the 1.02 μs via vertical dashed lines. On the right, we plot only the $t_p = 1.02$ μs $\pi/2$ -pulse to emphasize that the rise-time portion of the pulse makes up about 12.5% of the total duration, whereas the fall-time portion is extremely rapid by comparison.

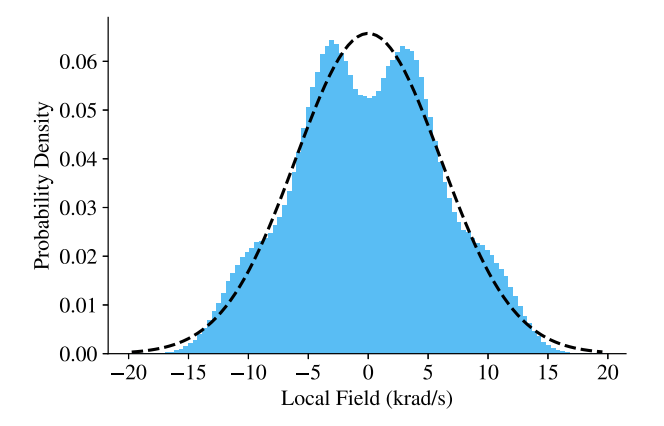


Fig. B.7. Disordered field distribution for a fluorine spin, as generate by neighboring phosphorus spins. The crystal is approximated as a cubic cluster of 27 neighboring unit cells containing 6 phosphorus atoms each. To avoid computing all 2²¹⁶ possible configurations, we randomly sample 10⁶ configurations, where each spin is equally likely to be up or down.

Now, it remains to do the quenched disorder average. Experimentally, this happens naturally within a single scan, given that our measured signal is the average of a macroscopic number of nuclei. By Monte Carlo techniques, one can estimate the distribution of the disordered field by randomly sampling phosphorus nuclear spin orientations and computing the resulting mean field for each configuration. This technique leads to a multimodal distribution which is well approximated by a single Gaussian, with zero mean and standard deviation of $\sigma_h = 6.069$ krad s⁻¹, shown in Fig. B.7. Then, averaging over the disorder distribution, we conclude that

$$\overline{\left\langle \hat{S}_{z}(t)\hat{S}_{z}\right\rangle} \propto \frac{1}{2} \int_{-\infty}^{\infty} dh_{i} \left(1 + \cos\frac{\sqrt{2}h_{i}t}{3}\right) \frac{1}{\sqrt{2\pi}\sigma_{h}} e^{-\frac{n_{i}^{2}}{2\sigma_{h}^{2}}}$$

$$= \frac{1}{2} + \frac{1}{2} e^{-\frac{1}{9}(\sigma_{h}t)^{2}}.$$
(B.7)

In general, if $h_i \sim X$ for arbitrary probability distribution X, then the Gaussian term is replaced by the characteristic function of X,

$$\overline{\left\langle \hat{S}_{z}(t)\hat{S}_{z}\right\rangle} \propto \frac{1}{2} + \frac{1}{2}\operatorname{Re}\left(\phi_{X}\left(\frac{\sqrt{2}}{3}t\right)\right).$$
 (B.8)

Here, the characteristic function is defined as $\phi_X(t) = \mathbb{E}[\exp(itX)]$.

The true distribution is clearly not a Gaussian, with details that may be computationally intractable to access. However, we can still extract descriptive statistics analytically. Consider the distribution of a generalized locally disordered field, $\{h_i\}$. Motivated by Eq. (B.1), and under the assumption of quenched disorder, each spin operator $\hat{I}_z^{(j)}$ will contribute only a single eigenvalue to a given disorder instance.

Hence, we are able to replace the spin operator $\hat{I}_z^{(j)}$ with a classical random variable, I_j . Then, the disordered field distribution is given by the formal sum.

$$h_i = \sum_{i} J_{ij}^{FP} I_j. \tag{B.9}$$

For an infinite temperature system, I_j is uniformly random with outcomes depending on the underlying nuclear spin species.

Let s_j be the total spin of nucleus j. In a thermal ensemble consisting of a single spin species at infinite temperature, all I_j are independent and identically distribution uniform random variables with outcomes given by the set of spin eigenvalues, $\{-s_j, -s_j+1, \ldots, s_j\}$. Thus, the mean is easily seen to be

$$\mathbb{E}[I_i] = 0, \tag{B.10}$$

by symmetry. The second moment is given by

$$\mathbb{E}[I_j^2] = \frac{1}{2s_j + 1} \sum_{i = -s_j}^{s_j} i^2 = \frac{2s_j(s_j + 1)(2s_j + 1)}{6(2s_j + 1)} = \frac{s_j(s_j + 1)}{3},$$
 (B.11)

which holds regardless of whether s_i is integer or half-integer.

Using the above information, we can compute descriptive statistics of the disordered field variable h_i . The mean of the local disordered field distribution is 0 by linearity of the expectation value:

$$\mu = \mathbb{E}[h_i] = \mathbb{E}\left[\sum_j J_{ij}^{FP} I_j\right] = \sum_j J_{ij}^{FP} \mathbb{E}[I_j] = 0.$$

Moreover, we can compute the variance:

$$\begin{split} (\Delta h_i)^2 &= \mathbb{E}[h_i^2] - \mathbb{E}[h_i]^2 = \mathbb{E}[h_i^2] \\ &= \mathbb{E}\left[(\sum_j J_{ij}^{FP} I_j)^2 \right] = \mathbb{E}\left[\sum_{j,k} J_{ij}^{FP} J_{ik}^{FP} I_j I_k \right] \\ &= \sum_j (J_{ij}^{FP})^2 \mathbb{E}[I_j^2] + \sum_{j \neq k} J_{ij}^{FP} J_{ik}^{FP} \mathbb{E}[I_j I_k] \\ &= \frac{1}{3} \sum_j (J_{ij}^{FP})^2 (s_j) (s_j + 1). \end{split}$$
(B.12)

Above, we utilized the fact that each I_j is i.i.d., so that for $j \neq k$, $\mathbb{E}[I_i I_k] = \mathbb{E}[I_j] \mathbb{E}[I_k] = 0$.

Connecting these results back to the main text, we focus on measurements of fluorapatite, such that $\hat{I}_z^{(j)}$ are spin operators associated with phosphorous-31 spins, hence all $s_j = \frac{1}{2}$. By translational symmetry the index i can be suppressed, and we compute

$$\sigma_h^2 = (\Delta h_i)^2 = \frac{1}{4} \sum_j (J_{ij}^{FP})^2.$$
 (B.13)

Since the dipolar coupling strength falls off as r^{-3} , $(J_i^{FP})^2 \sim |i-j|^{-6}$ and will certainly converge for any 3-dimensional crystal.

Numerically, we can compute σ_h exactly for a crystal composed of a finite number of unit cells. Then, in the infinite scaling limit with

an r^{-3} power law, we estimate $\sigma_h = 5.84826$ krad s⁻¹. From exact computations with crystal sizes on the order of 10^4 unit cells, we find that the difference between the infinite system estimate and finite size computations is on the order of milliradians per second. These computations are qualitatively consistent with the Gaussian estimation from the Monte Carlo reconstruction of the disorder distribution.

For the case $s_j=1/2, \forall j$, we can extend this result to finite temperatures. In this case, we have that secondary spin species is in a Gibbs state with inverse temperature β with respect to the Zeeman Hamiltonian for a paramagnetic spin species, $\mathcal{H}=-\hbar\omega\hat{I}_z$. The first two moments are straightforward to compute:

$$\mathbb{E}[I_j] = \left\langle \hat{I}_z^{(j)} \right\rangle_{\beta} = \frac{1}{2} \tanh \frac{\beta \hbar \omega}{2},\tag{B.14}$$

$$\mathbb{E}[I_j^2] = \frac{1}{4} \langle \mathbb{1} \rangle_{\beta} = \frac{1}{4}. \tag{B.15}$$

Using the above single-spin expectation values, we can compute descriptive statistics of the disordered field. For non-zero β , the mean is also non-zero,

$$\mu = \frac{1}{2} \tanh \frac{\beta \hbar \omega}{2} \sum_{j} J_{ij}^{FP}$$
 (B.16)

The variance is similarly modified,

$$(\Delta h_i)^2 = \sum_j J_{ij}^2 (\Delta I_j)^2.$$
 (B.17)

It is easy to see that

$$(\Delta I_j)^2 = \frac{1}{4} \left(1 - \tanh^2 \frac{\beta \hbar \omega}{2} \right) = \frac{1}{4} \operatorname{sech}^2 \frac{\beta \hbar \omega}{2}.$$
 (B.18)

Thus

$$\sigma_h^2 = \frac{1}{4} \operatorname{sech}^2 \frac{\beta \hbar \omega}{2} \sum_{i} (J_{ij})^2.$$
 (B.19)

Indeed, for $\beta=0$, variance simplifies to the infinite temperature result. It is instructive to consider a small parameter expansion in $\zeta\equiv\frac{\beta\hbar\omega}{2}$. Here, ζ is unit-less, taking values of $\zeta\approx1.5\times10^{-6}$ for phosphorus-31 at room temperature in a 7.1 T magnet. Hence, we can confidently employ small angle approximations $\tanh(\zeta)=\zeta+O(\zeta^3)$ and $\mathrm{sech}^2(\zeta)=1-\zeta^2+O(\zeta^4)$. We see that our infinite temperature approximation is sufficient, as the leading order corrections are still quite small:

$$\mu = \frac{\zeta}{2} \sum_{j} J_{ij}^{FP} + O(\zeta^{3})$$

$$\sigma_{h}^{2} = \frac{1 - \zeta^{2}}{4} \sum_{i} (J_{ij}^{FP})^{2} + O(\zeta^{4})$$

Note that while at first glance $\sum_j J_{ij}^{FP}$ looks to be logarithmically divergent, we argue that it converges. Upgrading to continuous spherical coordinates (r,θ,ϕ) , $J_{ij}^{FP} \longrightarrow J(r,\theta,\phi) \propto (1-3\cos^2\theta)/r^3$ where θ is the azimuthal angle. Notice $\langle 1-3\cos^2\theta \rangle = 0$ on a spherical shell for uniformly distributed θ . With increasing r, the lattice points will fill a shell, $[r,r+\delta r)$, with increasing uniformity and approach 0. As such $\sum_j J_{ij}^{FP}$ converges quickly to a value of about 19 krad s⁻¹, which we computed numerically. When multiplied by $\frac{\zeta}{2}$ this results in a disorder mean of $\mu=0.015$ rad s⁻¹. In our experiments, this value is indistinguishable from 0.

Appendix C. Supplementary information: Hamiltonian engineering

In this work, we considered the solid-state nuclear magnetic resonance of fluorapatite, $Ca_5(PO_4)_3F$, in a 300 MHz Bruker spectrometer. The crystal is placed with the magnetic field aligned along its c axis, where the intrachain coupling is approximately 40 times larger than the interchain coupling [24,29,30]. Within the rotating frame generated by the magnetic field, our system Hamiltonian has three main components: dipolar z, locally disordered z, and collective control.

$$\mathcal{H}(t) = \mathcal{H}_{Dz} + \mathcal{H}_{dis} + \mathcal{H}_{c}(t), \tag{C.1}$$

Concretely, each component of the Hamiltonian is:

$$\begin{split} \mathcal{H}_{Dz} &= \frac{1}{2} \sum_{i < j} J_{ij}^{FF} \left(2 \hat{S}_{z}^{(i)} \hat{S}_{z}^{(j)} - (\hat{S}_{x}^{(i)} \hat{S}_{x}^{(j)} + \hat{S}_{y}^{(i)} \hat{S}_{y}^{(j)}) \right) \\ \mathcal{H}_{dis} &= \sum_{i,j} J_{ij}^{FP} \hat{S}_{z}^{(i)} \hat{I}_{z}^{(i)} \approx \sum_{i} h_{i} \hat{S}_{z}^{(i)} \\ \mathcal{H}_{c}(t) &= f(t) \left(\cos(\phi) \hat{S}_{x} + \sin(\phi) \hat{S}_{y} \right), \end{split}$$

where

$$J_{ij}^{FF} = \frac{\hbar^2 \gamma_F^2 (1 - 3\cos^2(\theta_{ij}))}{\left\| r_i - r_j \right\|^3}.$$
 (C.2)

is the homonuclear fluorine dipolar coupling strength. In fluorapatite, when the magnetic field is aligned along the crystal's c-axis, the system is well described as an ensemble of one dimensional spin chains. In this case it is sufficient to focus on coupling within a chain, so that $J_{i,i+r}^{FF} = J_0^{FF}/r^3 \, (J_0^{FF} \approx -33 \, {\rm krad \, s^{-1}})$. The heteronuclear coupling, J_{ij}^{FP} , was previously defined in Eq. (B.2). For simplicity, we have introduced the collective spin operators,

$$\hat{S}_{\mu} = \frac{1}{2} \sum_{i} \sigma_{\mu}^{(i)}, \quad \mu \in \{x, y, z\}.$$
 (C.3)

As discussed in the main text, $\mathcal{H}_c(t)$ is idealized, wherein f(t) is a square pulse at fixed power so that the net effect of each control pulse is a $\pi/2$ rotation about a fixed axis determined by ϕ . In our system, ϕ has a resolution of one degree, and is fixed during the duration of a pulse.

Within the main text, we utilized a variety of multi-pulse sequences, including Wei16, Angle12, Peng24, and MREV-8. Here, we provide the pulse sequences and resulting time averaged Hamiltonians for all experiments considered.

To begin, Wei16 is a 16-pulse sequence, composed of four similarly structured 4-pulse blocks [31]. Unless otherwise specified, a pulse corresponds to a $\pi/2$ rotation about a particular transverse axis of the Bloch sphere obtained by turning on the rf driving for a time t_p , which in this work takes values $t_p \in \{1.02, 1.52, 2.02\}$ µs. Each 4-pulse block corresponds to $6\tau_0$ of time, where $\tau_0 = 5$ µs is the delay primitive for the entire sequence. It is prudent to choose τ_0 to be as short as possible in order to minimize Trotter errors while still ensuring interpulse delays $\tau_0 - t_p$ are not too short. For our spectrometer, $\tau_0 = 5$ µs is as short as feasible, given that the electronics require a minimum pulse separation of 2.5 µs to change the phase for the next applied pulse. For case where $t_p = 2.02$ µs, τ_0 must be extended to 6 µs.

Under Wei16, the internal Hamiltonian can be transformed to a model with 6 free parameters, 3 controlling the interaction Hamiltonian and 3 controlling the orientation of the local field. Notably, with collective rotations we cannot change the sum of the coefficients of the interaction Hamiltonian, since the subspace generated by the dipolar interaction along x, y, and z, written span{ $\mathcal{H}_{D_x}, \mathcal{H}_{D_y}, \mathcal{H}_{D_z}$ }, is a two-dimensional vector space. This can be seen clearly by recalling one of the central identities used to perform time suspension, $\mathcal{H}_{D_x} + \mathcal{H}_{D_y} + \mathcal{H}_{D_z} = 0$. The constraint is directly captured in the Floquet Hamiltonian, defined below.

$$\mathcal{H}_{F} = \frac{1}{2} \sum_{i < j} J_{ij} \left((u - w) \hat{S}_{x}^{(i)} \hat{S}_{x}^{(j)} + (v - u) \hat{S}_{y}^{(i)} \hat{S}_{y}^{(j)} + (w - v) \hat{S}_{z}^{(i)} \hat{S}_{z}^{(j)} \right)$$

$$+ \frac{1}{3} \sum_{i} \omega_{i} \left(a \hat{S}_{x}^{(i)} + b \hat{S}_{y}^{(i)} + c \hat{S}_{z}^{(i)} \right). \tag{C.4}$$

Each of the parameters appearing above are combined to produced the physical pulse delays for the sequence, given below.

$$\begin{split} \tau_1 &= \tau_0 (1+c-v+w), & \tau_2 &= \tau_0 (1+b-u+v), & \tau_3 &= \tau_0 (1-a+u-w) \\ \tau_1' &= \tau_0 (1-c-v+w), & \tau_2' &= \tau_0 (1-b-u+v), & \tau_3 &= \tau_0 (1+a+u-w). \end{split}$$

In general, a four-pulse sequence is defined by five delays and four orientations, which we collect using the following notation, $P(t_1, n_1, t_2, n_2, t_3, n_3, t_4, n_4, t_5)$; a standard notation for our group [31,32]. Unlike strings of unitary operators, this notation is read left-to-right, in the

order they are physically applied during an experiment. Namely, the generic pulse sequence corresponds to "wait for t_1 , then apply a pulse in the n_1 direction, then wait for t_2, \ldots " and so on. Concretely, the Wei16 sequence is given by the string of four pulse blocks shown below.

$$P(\tau_{1}, \mathbf{x}, \tau_{2}, \mathbf{y}, 2\tau_{3}, \mathbf{y}, \tau'_{2}, \mathbf{x}, \tau'_{1})P(\tau'_{1}, \mathbf{x}, \tau_{2}, \mathbf{y}, 2\tau'_{3}, \mathbf{y}, \tau'_{2}, \mathbf{x}, \tau_{1}) \cdots P(\tau_{1}, \bar{\mathbf{x}}, \tau'_{2}, \bar{\mathbf{y}}, 2\tau'_{2}, \bar{\mathbf{y}}, \tau_{2}, \bar{\mathbf{x}}, \tau'_{1})P(\tau'_{1}, \bar{\mathbf{x}}, \tau'_{2}, \bar{\mathbf{y}}, 2\tau_{3}, \bar{\mathbf{y}}, \tau_{2}, \bar{\mathbf{x}}, \tau_{1})$$

Here we use the standard notation $\bar{x} = -x$, which helps save horizontal space. In this sequence, there is a great deal of reflection symmetry. Generally, symmetrized pulse sequences perform better than their unsymmetrized counterparts, which can be formalized by computing leading-order error term.

The Peng24 sequence differs from Wei16 in that it is constructed by symmetrizing a pulse sequence reliant on a three-fold symmetry, which differs significantly from the usual two-fold symmetry four-pulse blocks demonstrated above. Additionally, as a time suspension sequence, the target Hamiltonian is much simpler, $\mathcal{H}_F=0$. In particular, we chose Peng24 as it is a 24-pulse sequence corresponding to $24\tau_0$ of evolution time, equivalent to that of Wei16, allowing for a direct comparison. We can write Peng24 in the same way we did Wei16, taking the standard pulse block to include three orientations and four delays in order to better emphasize the symmetry group. Since Peng24 is symmetrized Angle12, we define Angle12 below and make concrete how it is used to define Peng24 (first introduced as yxx24) [5].

$$\begin{split} & \text{Angle12} = P\left(\frac{\tau_0}{2}, \bar{\pmb{y}}, \tau_0, \pmb{x}, \tau_0, \bar{\pmb{x}}, \frac{\tau_0}{2}\right) P\left(\frac{\tau_0}{2}, \pmb{y}, \tau_0, \bar{\pmb{x}}, \tau_0, \bar{\pmb{x}}, \frac{\tau_0}{2}\right) \cdots \\ & P\left(\frac{\tau_0}{2}, \bar{\pmb{y}}, \tau_0, \pmb{x}, \tau_0, \bar{\pmb{x}}, \frac{\tau_0}{2}\right) P\left(\frac{\tau_0}{2}, \pmb{y}, \tau_0, \pmb{x}, \tau_0, \pmb{x}, \frac{\tau_0}{2}\right) \end{split}$$

As stated, Peng24 is formed by symmetrizing Angle12, which is done by performing Angle12, followed by $\overline{\text{Angle12}}$. The overbar on Angle12 means to perform Angle12, albeit with the signs of each pulse orientation reversed, $x \longrightarrow \bar{x}$ etc. Hence,

$$Peng24 = Angle12 \overline{Angle12}.$$
 (C.5)

Finally, we review the 8-pulse sequence MREV-8 given by the following series of pulses [33]:

$$\text{MREV-8} = P(\tau_0, \bar{\mathbf{x}}, \tau_0, \mathbf{y}, 2\tau_0, \bar{\mathbf{y}}, \tau_0, \mathbf{x}, \tau_0) P(\tau_0, \mathbf{x}, \tau_0, \mathbf{y}, 2\tau_0, \bar{\mathbf{y}}, \tau_0, \bar{\mathbf{x}}, \tau_0).$$
(C.6)

In addition to decoupling the dipolar interaction of the fluorine atoms, MREV-8 alters the magnitude and direction of the disordered field, with a resulting Floquet Hamiltonian of

$$\mathcal{H}_{MREV} = \frac{1}{3} \sum_{i} h_i \left(\hat{S}_x^{(i)} + \hat{S}_z^{(i)} \right).$$
 (C.7)

Other 8-pulse spectral sequences can produce different orientations of the disordered field, such as WAHUHA-8 [34], which leaves the disordered field orientation unchanged, albeit similarly re-scaled in magnitude.

References

- [1] J.S. Waugh, L.M. Huber, U. Haeberlen, Approach to high-resolution NMR in solids, Phys. Rev. Lett. 20 (5) (1968) 180.
- [2] U. Haeberlen, High Resolution NMR in solids selective averaging: supplement 1 advances in magnetic resonance, vol. 1, Elsevier, 1976.
- [3] E.S. Mananga, T. Charpentier, On the floquet-magnus expansion: Applications in solid-state nuclear magnetic resonance and physics, Phys. Rep. 609 (2016) 1–49.
- [4] P. Mansfield, Symmetrized pulse sequences in high resolution NMR in solids, J. Phys. C 4 (11) (1971) 1444.

- [5] P. Peng, X. Huang, C. Yin, L. Joseph, C. Ramanathan, P. Cappellaro, Deep reinforcement learning for quantum Hamiltonian engineering, Phys. Rev. A 18 (2022) 024033, http://dx.doi.org/10.1103/PhysRevApplied.18.024033, URL https://link.aps.org/doi/10.1103/PhysRevApplied.18.024033.
- [6] M.M. Maricq, Application of average Hamiltonian theory to the NMR of solids, Phys. Rev. B 25 (11) (1982) 6622.
- [7] M. Heyl, P. Hauke, P. Zoller, Quantum localization bounds trotter errors in digital quantum simulation, Sci. Adv. 5 (4) (2019) eaau8342.
- [8] L.M. Sieberer, T. Olsacher, A. Elben, M. Heyl, P. Hauke, F. Haake, P. Zoller, Digital quantum simulation, trotter errors, and quantum chaos of the kicked top, npj Quant. Inf. 5 (1) (2019) 78.
- [9] M. Mehring, J.S. Waugh, Phase transients in pulsed NMR spectrometers, Rev. Sci. Instrum. 43 (4) (1972) 649–653.
- [10] J. Ellett Jr., M. Gibby, U. Haeberlen, L. Huber, M. Mehring, A. Pines, J. Waugh, Spectrometers for multiple-pulse NMR, in: Advances in Magnetic and Optical Resonance, Vol. 5, Elsevier, 1971, pp. 117–176.
- [11] T.M. Barbara, J.F. Martin, J.G. Wurl, Phase transients in NMR probe circuits, J. Magnet. Reson. (1969) 93 (3) (1991) 497–508.
- [12] H.Y. Carr, E.M. Purcell, Effects of diffusion on free precession in nuclear magnetic resonance experiments, Phys. Rev. 94 (3) (1954) 630.
- [13] A. Maudsley, Modified carr-purcell-meiboom-gill sequence for NMR fourier imaging applications, J. Magnet. Reson. (1969) 69 (3) (1986) 488–491.
- [14] A.M. Souza, G.A. Álvarez, D. Suter, Robust dynamical decoupling, Phil. Trans. R. Soc. A 370 (1976) (2012) 4748–4769.
- [15] J.J. Wittmann, K. Takeda, B.H. Meier, M. Ernst, Compensating pulse imperfections in solid-state NMR spectroscopy: A key to better reproducibility and performance, Ang. Chem. Int. Ed. 54 (43) (2015) 12592–12596.
- [16] A.J. Vega, Controlling the effects of pulse transients and RF inhomogeneity in phase-modulated multiple-pulse sequences for homonuclear decoupling in solid-state proton NMR, J. Magn. Reson. 170 (1) (2004) 22–41.
- [17] Y. Tabuchi, M. Negoro, K. Takeda, M. Kitagawa, Total compensation of pulse transients inside a resonator, J. Magn. Reson. 204 (2) (2010) 327–332.
- [18] J. Weber, M. Seemann, J.S. auf der Günne, Pulse-transient adapted C-symmetry pulse sequences. Solid State Nucl. Magn. Reson. 43 (2012) 42–50.
- [19] K. Takeda, Y. Tabuchi, M. Negoro, M. Kitagawa, Active compensation of rf-pulse transients, J. Magn. Reson. 197 (2) (2009) 242–244.
- [20] I. Hincks, C. Granade, T.W. Borneman, D.G. Cory, Controlling quantum devices with nonlinear hardware, Phys. Rev. A 4 (2) (2015) 024012.
- [21] T.W. Borneman, D.G. Cory, Bandwidth-limited control and ringdown suppression in high-Q resonators, J. Magn. Reson. 225 (2012) 120–129.
- [22] D.C. McKay, C.J. Wood, S. Sheldon, J.M. Chow, J.M. Gambetta, Efficient Z gates for quantum computing, Phys. Rev. A 96 (2) (2017) 022330.
- [23] E. Knill, R. Laflamme, R. Martinez, C.-H. Tseng, An algorithmic benchmark for quantum information processing, Nature 404 (6776) (2000) 368–370.
- [24] K.X. Wei, C. Ramanathan, P. Cappellaro, Exploring localization in nuclear spin chains, Phys. Rev. Lett. 120 (2018) 070501, http://dx.doi.org/10.1103/PhysRevLett.120.070501, URL https://link.aps.org/doi/10.1103/PhysRevLett.120.070501.
- [25] M. Suzuki, Decomposition formulas of exponential operators and Lie exponentials with some applications to quantum mechanics and statistical physics, J. Math. Phys. 26 (4) (1985) 601–612.
- [26] U. Haeberlen, J.S. Waugh, Coherent averaging effects in magnetic resonance, Phys. Rev. 175 (1968) 453–467, http://dx.doi.org/10.1103/PhysRev.175.453, URL https://link.aps.org/doi/10.1103/PhysRev.175.453.
- [27] T. Gorin, T. Prosen, T.H. Seligman, M. Žnidarič, Dynamics of loschmidt echoes and fidelity decay, Phys. Rep. 435 (2–5) (2006) 33–156.
- [28] A. Stasiuk, P. Cappellaro, Observation of a prethermal U(1) discrete time crystal, Phys. Rev. X 13 (2023) 041016, http://dx.doi.org/10.1103/PhysRevX. 13.041016, URL https://link.aps.org/doi/10.1103/PhysRevX.13.041016.
- [29] P. Cappellaro, C. Ramanathan, D.G. Cory, Simulations of information transport in spin chains, Phys. Rev. Lett. 99 (25) (2007) 250506.
- [30] W. Zhang, P. Cappellaro, N. Antler, B. Pepper, D.G. Cory, V.V. Dobrovitski, C. Ramanathan, L. Viola, NMR multiple quantum coherences in quasi-onedimensional spin systems: Comparison with ideal spin-chain dynamics, Phys. Rev. A 80 (5) (2009) 052323.
- [31] K.X. Wei, C. Ramanathan, P. Cappellaro, Exploring localization in nuclear spin chains. Phys. Rev. Lett. 120 (7) (2018) 070501.
- [32] P. Peng, B. Ye, N.Y. Yao, P. Cappellaro, Exploiting disorder to probe spin and energy hydrodynamics, Nat. Phys. (2023) 1–6.
- [33] P. Mansfield, M.J. Orchard, D.C. Stalker, K.H.B. Richards, Symmetrized multipulse nuclear-magnetic-resonance experiments in solids: Measurement of the chemical-shift shielding tensor in some compounds, PRB 7 (1) (1973) 90, http://dx.doi.org/10.1103/PhysRevB.7.90.
- [34] J. Waugh, L. Huber, U. Haeberlen, Approach to high-resolution NMR in solids, Phys. Rev. Lett. 20 (1968) 180, http://dx.doi.org/10.1103/PhysRevLett.20.180.